Supplementary Materials for

Robust Flat-Magnetoresistivity in a 3D Nodal Flat-band Semimetal

Ruoqi Wang[1,2], Xin Gu[1,2], Haofu Wen[1,2], Bo Zhao[3,4] , Shijun Yuan[1,2], Mingliang Wu[1,2], Langsheng Ling[5], Chuanying Xi[5], Kunquan Hong[1,2], Ke Xia[2]*, Taishi Chen[1,2]*, Jinlan Wang[1,2]

1. *Key Laboratory of Quantum Materials and Devices of Ministry of Education,*
2. *School of Physics, Southeast University, Nanjing 211189, China*
3. *Shanghai Advanced Research Institute, CAS 239 Zhangheng Road, Pudong, Shanghai 201204, China.*
4. *Henan Key Laboratory of Imaging and Intelligent Processing Zhengzhou, China*
5. *High Magnetic Field Laboratory Chinese Academy of Sciences, Hefei 230031, China*

Ruoqi Wang, Xin Gu, Haofu Wen, and Bo Zhao contributed equally.

*Corresponding author. E-mail: chentaishi@seu.edu.cn, kexia@seu.edu.cn

S1. THE SCALING PLOT FOR THE $|\sigma_{xy}|$ *VERSUS* σ_{xx} IN Fe_3Ga

Intrinsic AHE originates from the Bloch electrons' scattering[1,2]. The intrinsic AHC $\sigma_{xy}^{\text{int.}}$ at a finite temperature is expressed as: $\sigma_{xy}^{\text{int.}} = -\frac{e^2}{h}\sum_{n,\mathbf{k}}\int \frac{d\mathbf{k}}{2\pi^3} f(\varepsilon_n(\mathbf{k}))\Omega_{n,z}(\mathbf{k})$, where $\boldsymbol{f}\left(\boldsymbol{\varepsilon_n}(\mathbf{k})\right)$ and $\Omega_{n,z}(\mathbf{k})$ refer to the Fermi-Dirac distribution function and Berry curvature, respectively. The $\Omega_{n,z}(\mathbf{k})$ is given by $\Omega_{n,\mu\upsilon}(\mathbf{k}) = i\sum_{n' \neq n} \frac{<n'|\upsilon_\mu|n><n|\upsilon_\mu|n'>}{(\varepsilon_{n'}-\varepsilon_n)^2}$. Therefore, the $\sigma_{xy}^{\text{int.}}$ at finite temperature depends on the $\Omega_{n,z}(\mathbf{k})$. In the time-reversal-symmetry-breaking materials, such as ferromagnetic compounds, the integral of the Berry curvature over the first Brillouin zone leads to a nonzero Berry phase. When a nondegenerate band-crossing occurs, the Berry curvature increases significantly, leading to a large AHC on the order of 10^3 S/cm, even in antiferromagnetic compounds[1,3-6]. Generally, a material showing a giant AHC often indicates the existence of nodal points near its Fermi surface, making it as a highly effective strategy for exploring topological materials[7-10]. In the ferromagnetic metal, the Hall resistivity ρ_{xy} can be expressed as: $\rho_{xy} = R_0 B + R_S M_S$, where R_0, R_S, and M_S stand for the ordinary Hall coefficient, anomalous Hall coefficient and saturated magnetization[1,2,6,11], respectively. The intrinsic AHE resistivity, $\rho_{xy}^{\text{intr}} = R_S M_S$, is quadratically proportional to the resistivity ρ_{xx}, namely $\rho_{xy}^{\text{intr}} \propto \rho_{xx}^2$. Using the tensor relations of resistivity, $\sigma_{\mathbf{xy}} = \frac{-\rho_{\mathbf{xy}}}{\rho_{\mathbf{xy}}^2 + \rho_{\mathbf{xx}}^2}$, $|\sigma_{xy}^{\text{int.}}|$ behaves as a constant, independent of σ_{xx}, resulting in the scaling relation: $|\sigma_{xy}^{\text{int.}}| \propto \sigma_{xx}^0$.

The scaling plot for the $|\sigma_{\mathbf{xy}}|$ versus σ_{xx} in Fe_3Ga is shown in Supplementary Fig. 8. Due to the high isotropy in magnetic crystalline and the nodal-web in Fe_3Ga, the AHC shows very small diversity under different measurement configurations[7]. This is very different from the scenario in hexagonal topological magnets such as Mn_3Sn and $Co_3Sn_2S_2$[3,4,6,12]. The giant $|\sigma_{\mathbf{xy}}|$ in all temperatures in Fig. 2b keeps constant in the intrinsic range, although the spin fluctuation dominates the MR at high temperatures. This strongly supports the $|\sigma_{\mathbf{xy}}|$ in Fe_3Ga originates from the nodal-web rather than extrinsic mechanisms, such as the side-jump[1,2]. Furthermore, the Fe_3Ga samples grown by the CVT method produce giant $|\sigma_{\mathbf{xy}}|$ more than twice larger than those grown by Czochralski method, despite their compositions being nearly identical. This can be attributed to the high quality of the CVT-grown Fe_3Ga samples. The Czochralski method grew samples faster than CVT method, but it often causes more defects. Compared the TEM images, we can clearly observe the satellite spots shown in the TEM image in *Ref.*7. In contrast, the patterns in this work are sharp and clean. The defects raising additional charge carriers adjusting the Fermi level have been well studied in the previous work[13].

S2. THE ESTIMATION OF THE AXIAL RELAXATION TIME

The axial relaxation time τ_A is an important factor when the chiral anomaly occurs, which represents the average time of fermions changing their handedness. In the simplified model, especially for the type-I Dirac and Weyl semimetals, the longitudinal conductivity σ_{xx}^{χ} under $\hat{\boldsymbol{B}} \parallel \hat{\boldsymbol{I}}$ is written as[14]:

$$\sigma_{xx}^{\chi} = \frac{e^2}{4\pi^2\hbar c}\frac{v}{c}\frac{(eB)^2 v^2}{\mu^2}\tau_A \qquad \text{(S1)}$$

from which τ_A can be expressed as:

$$\tau_A = \sigma_{xx}^{\chi}\frac{4\pi^2\hbar c}{e^2}\frac{c}{\upsilon}\frac{\mu^2}{(eB)^2 v^2} \qquad \text{(S2)}$$

namely,

$$\tau_A = \alpha \times 10^{60} \times \frac{\mu^2}{v^3} \qquad \text{(S3)}$$

where, the constants e, $\hbar$ and c are electron charge, reduced Planck constant and light velocity, and the υ, μ and B refer to the Fermi velocity, mobility and magnetic field, respectively. The α in (S3) is determined by fitting the positive magnetoconductivity induced by the chiral anomaly. The unit in the equation (S3) is second. The υ, μ can be determined by analyzing the quantum oscillations in the Dirac and Weyl semimetals. Therefore, τ_A can be easily obtained just by fit the positive magnetoconductivity for $\hat{\boldsymbol{B}} \parallel \hat{\boldsymbol{I}}$. However, by investigating the chiral-anomaly induced negative MR in well-known nodal semimetals (Table S1), the estimated τ_A reaches up to an order of 10^{48} s, much larger than the age of the universe we are living (4.32×10^{17} seconds according to the Big Bang Theory).

By looking into the formula (S1), we can also estimate the up-limit of σ_{xx}^{χ}, if we set τ_A, v to be the age of our universe and the light speed, and μ being in-between $1 \sim 0.001 m^2V^{-1}s^{-1}$, respectively. The yielded value is in the order of $1.67\times10^{-17}\,S\ cm^{-1}$ (for $\mu = 1 m^2V^{-1}s^{-1}$) $1.67\times10^{-11}\,S\ cm^{-1}$ ($\mu = 0.001 m^2V^{-1}s^{-1}$) when B=9 T, representing a very tiny correction to the longitudinal magnetoconductivity, which contradicts all reported chiral anomaly induced negative MRs[15-18].

In Fe_3Ga, we obtained the low-limit of τ_A by fitting the positive magnetoconductivity shown in the Supplementary Fig. 6, and the yielded values are in the order of 10^{30} s, if the μ and υ in equation (S3) are set as $0.001 m^2V^{-1}s^{-1}$ and $3\times10^8\,m/s$, respectively. The value remains very large.

In a word, the estimated τ_A values in so-far reported nodal semimetals are all incompatible with the experimental observations. In *Ref.*17, this obvious problem is attributed to the matrix element $\boldsymbol{M}$ in $1/\tau_A$, which was not well studied in *Refs.*14,19.

S3. DISCUSSIONS ON THE PLMR

In the theoretical consideration of the chiral anomaly induced PLMR[14,20], ρ_{Theory}^{PLMR} is written as:

$$\rho_{Theory}^{PLMR} = \rho_0 - \Delta\rho_\chi \cos^2(\theta - \frac{\pi}{2}) = \rho_0 - \frac{\Delta\rho_\chi}{2}\left[1 + \sin(2(\theta - \frac{\pi}{4}))\right] \quad \text{(S4)}$$

where the θ is defined in Fig. 3b. In this expression, $\theta = 0°$ and $90°$ refer to $\hat{\boldsymbol{B}} \perp \hat{\boldsymbol{I}}$ and $\hat{\boldsymbol{B}} \parallel \hat{\boldsymbol{I}}$, respectively. In real nodal semimetals[12,17,18], such as Na_3Bi, TaAs, WTe_2 and Co_2MnGa, etc., the MRs at cryogenic temperatures are positive for $\hat{\boldsymbol{B}} \perp \hat{\boldsymbol{I}}$, which is similar with the nodal-web ferromagnet Fe_3Ga. Consequently, the combination the positive and negative MR in PHE and PLMR do exist in Fe_3Ga, and gives rise to the flat-MR as shown in Fig. 3a in the main text. Therefore, the modified PLMR including both positive and negative MR is pressing needed.

$$\rho_{modified}^{PLMR} = \rho_0 - \Delta\rho_\chi \sin^2(2\theta - \frac{3\pi}{2}) \quad \text{(S5)}$$

Indeed, the modified formulas perfectly fit the PHE and PMLR in the main text.

S4. EXCLUDING THE CRYOGENIC AMR IN Fe_3Ga

To confirm the PLMR and PHE originating from the chiral anomaly, one must be cautious about the conventional AMR involved, as Fe_3Ga is a typical 3***d*** magnetic compound[21,22]. In conventional 3***d*** transition metals, the well-established formula for the planar AMR has been given[22]:

$$\rho_{Planar}^{AMR}(\frac{\pi}{2} - \theta) = \rho(0) + [\rho(\frac{\pi}{2}) - \rho(0)]\cos^2(\frac{\pi}{2} - \theta) \quad \text{(S6)}$$

where $\rho(0)$ and $\rho(\frac{\pi}{2})$ refer to the magnetoresistivity for $\hat{\boldsymbol{B}} \perp \hat{\boldsymbol{I}}$ and $\hat{\boldsymbol{B}} \parallel \hat{\boldsymbol{I}}$, respectively. Obviously, the formula (S6) shows the $\rho_{chiral\ anomaly}^{PLMR}$ shows the maximum for $\hat{\boldsymbol{B}} \perp \hat{\boldsymbol{I}}$ and the minimum under $\hat{\boldsymbol{B}} \parallel \hat{\boldsymbol{I}}$, while the $\rho_{3d\ Transition\ Metal}^{PHE}$ is totally opposite. The simulated $\rho_{chiral\ anomaly}^{PLMR}$ and $\rho_{3d\ Transition\ Metal}^{PHE}$ are shown in Supplementary Fig. 9 and Supplementary Fig. 10. In Fe_3Ga, the PMLR at 2 K is totally different from 300 K, which strongly supports the PHE and the PMLR below 50K originating from the chiral anomaly.

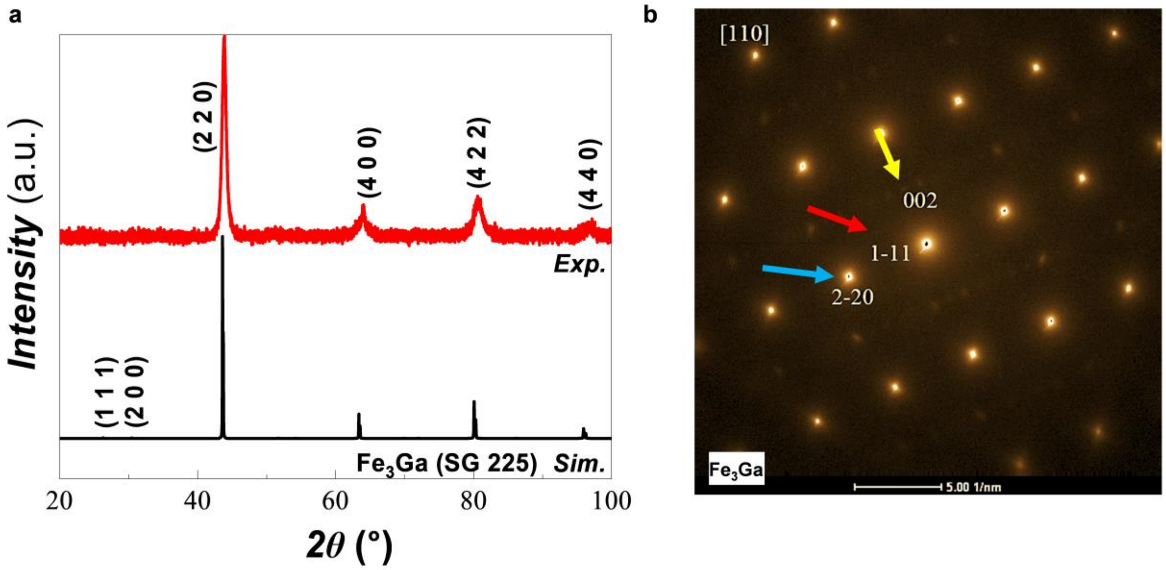

Supplementary Fig. 1. Powder XRD and TEM results for Fe_3Ga single crystals. a, The XRD result from the Fe_3Ga powder filed from single crystal Fe_3Ga grains. **b,** TEM image collected from the crystallographic [110] direction. The yellow, red and blue arrows refer to (002), $(1\bar{1}1)$ and $(2\bar{2}0)$, respectively.

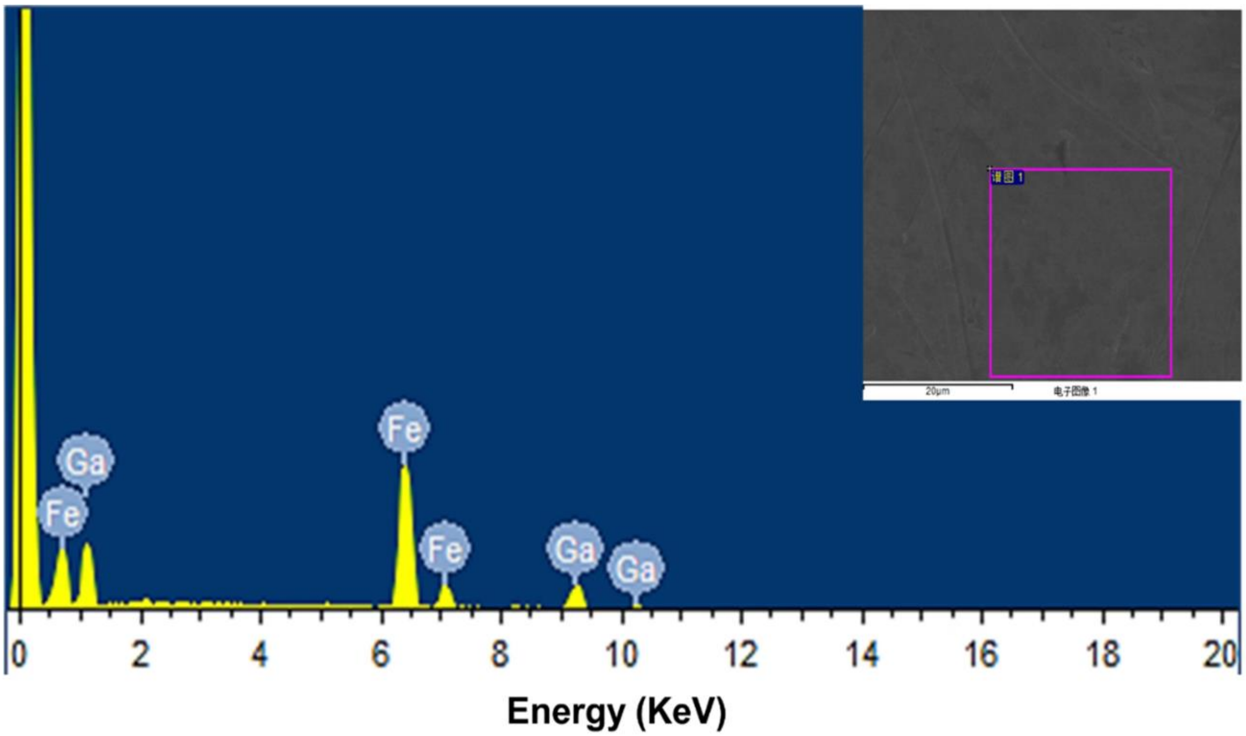

Supplementary Fig. 2. SEM/EDS analysis. The average atomic ratio over 10 spots on the polished bulk yields the composition of iron and gallium 3.07:0.97.

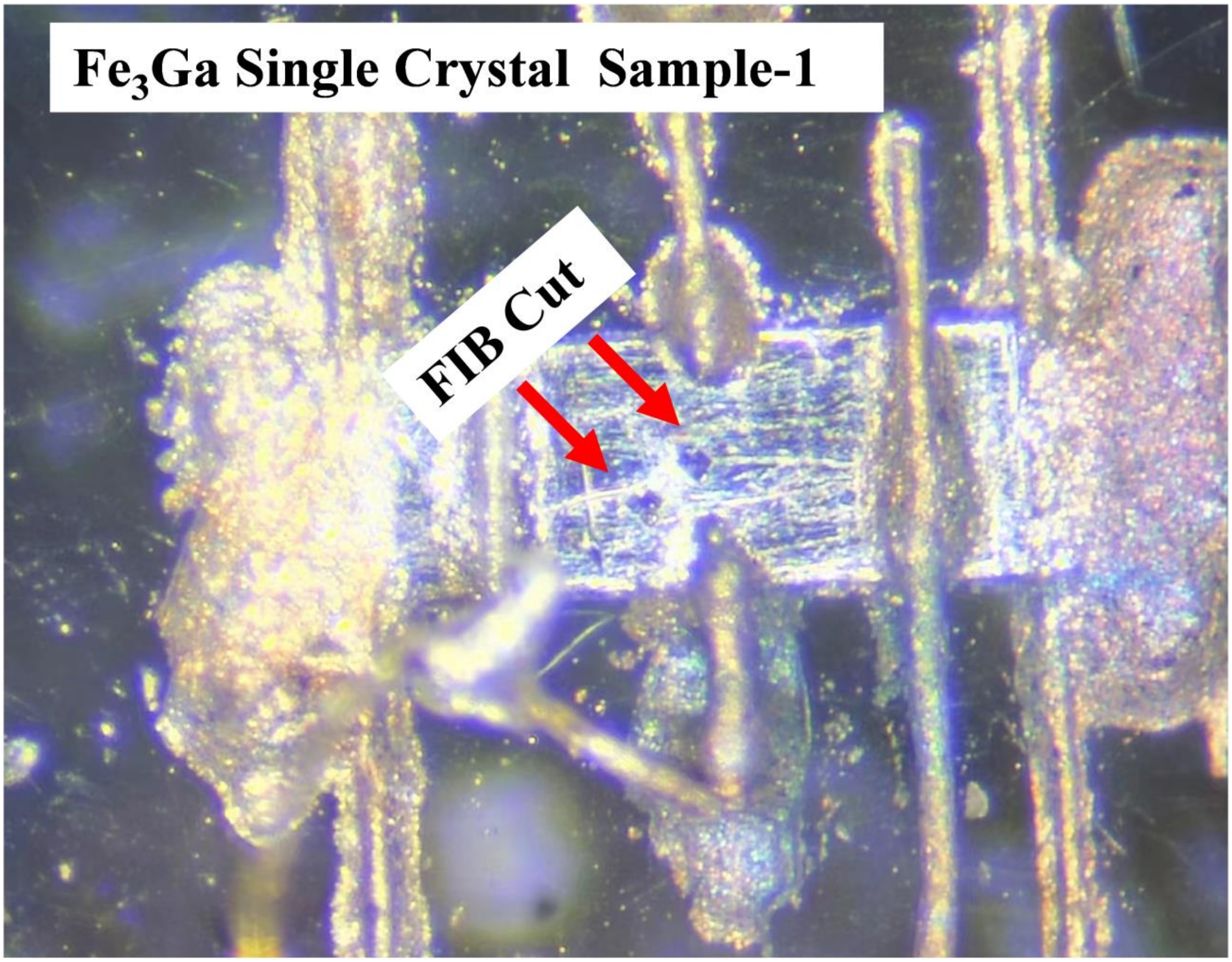

Supplementary Fig. 3. Fe_3Ga single crystal sample-1 studied in the main text. The two pits instructed by two arrows were made by a FIB-cut for TEM measurements, and these results are shown in Fig. 1c and Supplementary Fig. 1.

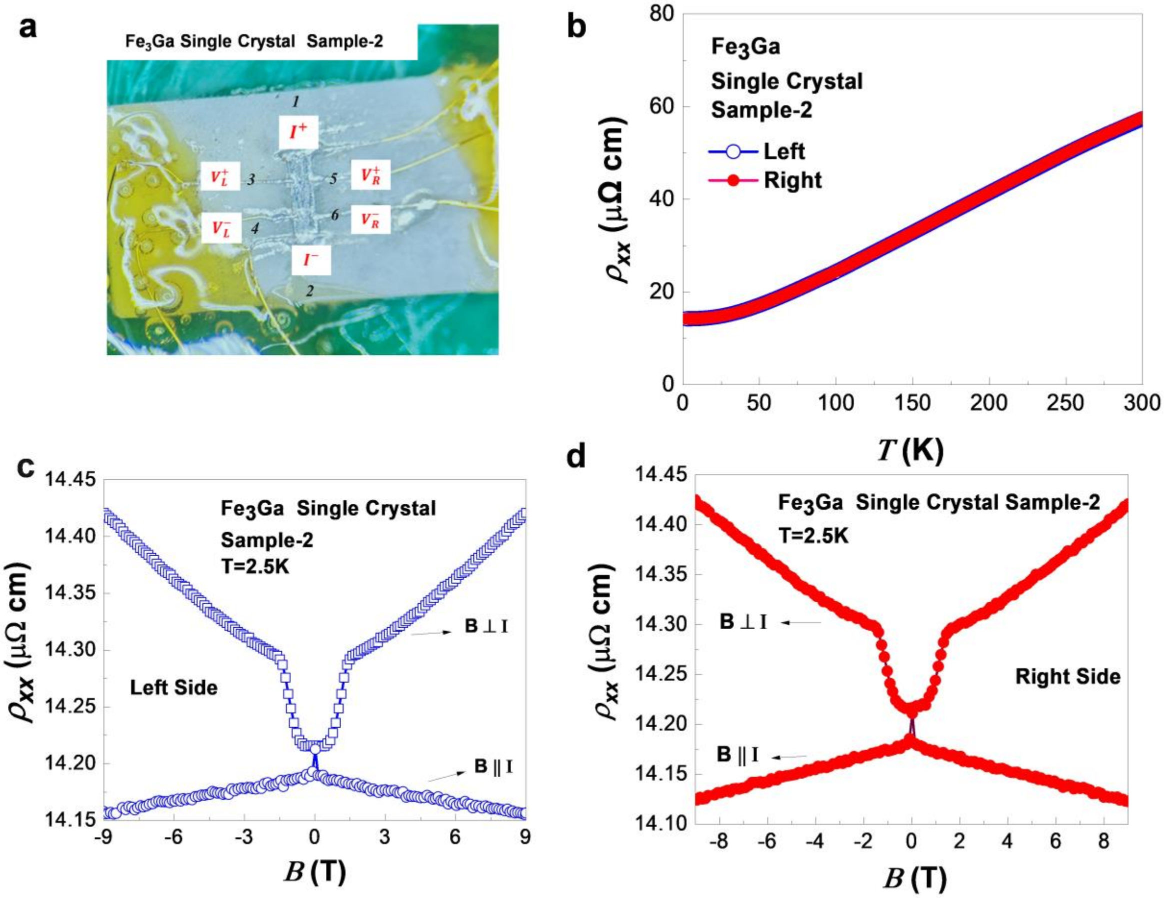

Supplementary Fig. 4. Excluding the inhomogeneous effect in Fe_3Ga single crystal sample-2. **a,** Six electric contacts were made along two sides. Contacts 1 and 2 were used for electron current -in and -out, respectively. The edge contacts 3 and 4 were used for longitudinal voltage drop collection on the left side, and the contacts 5 and 6 were used for longitudinal voltage collection on the right side. **b,** The RT curves for the left and right sides. **c,** and **d,** show the MR results for the left and right side under $\hat{\boldsymbol{B}} \perp \hat{\boldsymbol{I}}$ and $\hat{\boldsymbol{B}} \parallel \hat{\boldsymbol{I}}$, perfectly reproducing the results presented in the main text and excluding the current jetting effect in Fe_3Ga.

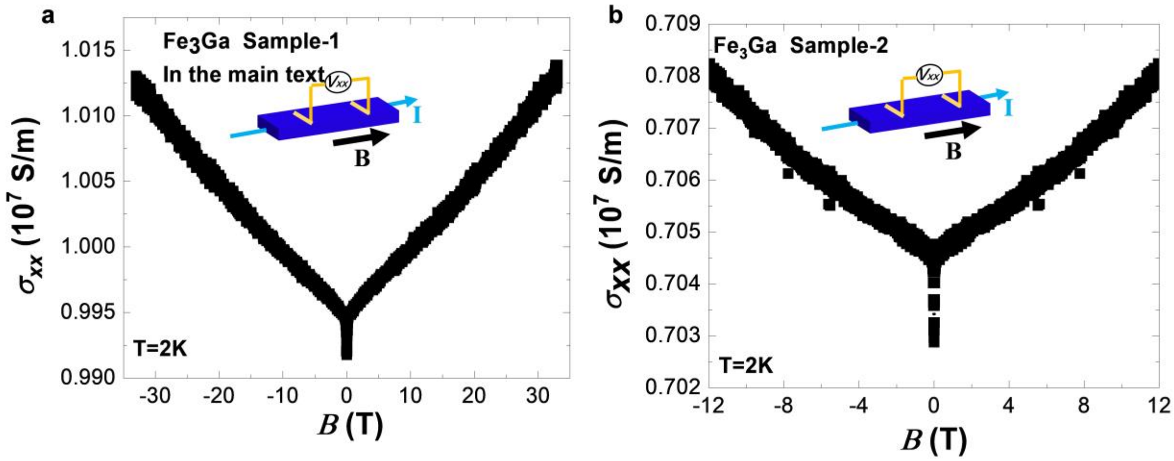

Supplementary Fig. 5. The chiral anomaly induced positive magnetoconductivity in Fe_3Ga single crystal sample-1 and sample-2. a, The positive magnetoconductivity in Fe_3Ga single crystal sample-1 under the configuration $\hat{\boldsymbol{B}} \parallel \hat{\boldsymbol{I}}$ at 2 K was measured up to 33 T by a steady high-magnetic field apparatus. **b,** The positive magnetoconductivity in Fe_3Ga single crystal sample-2 under $\hat{\boldsymbol{B}} \parallel \hat{\boldsymbol{I}}$ at 2 K.

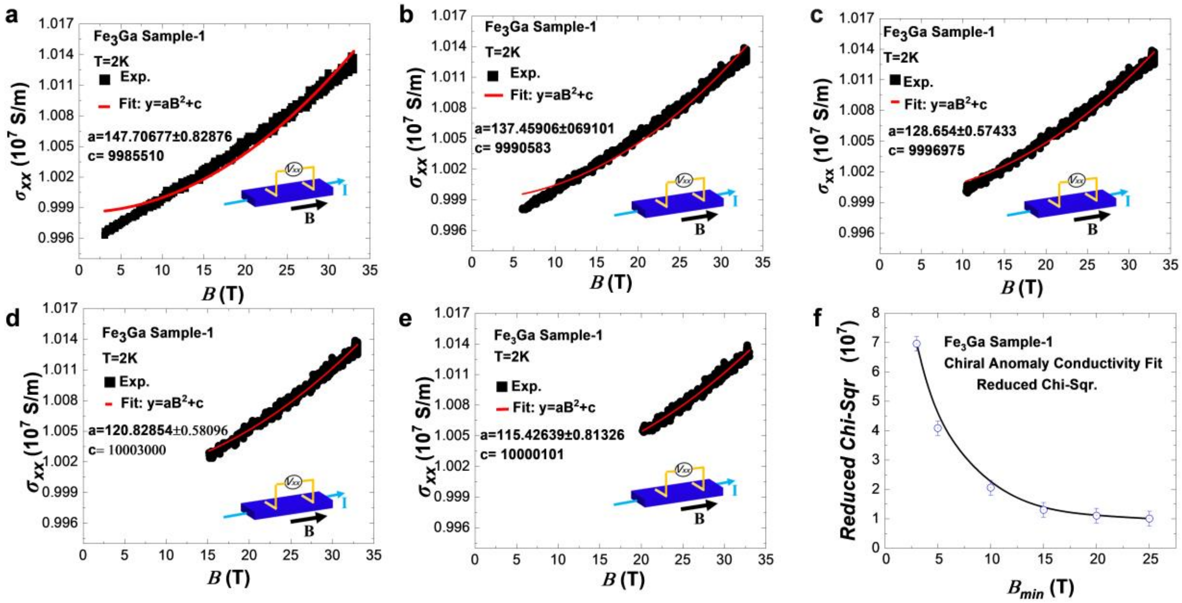

Supplementary Fig. 6. The fit on the magnetoconductivity in Fe_3Ga single crystal sample-1. The fit function is $y = aB^2 + c$. a, b, c, d and **e** refer to the results under the magnetic field range 3~33 T, 5~33 T, 10~33 T, 15~33 T and 20~33 T, respectively. **f,** shows the Reduced Chi-Sqr. verses minimum magnetic field ($B_{\min}$) for the fits. The smaller Reduced Chi-Sqr means the better fit results.

.

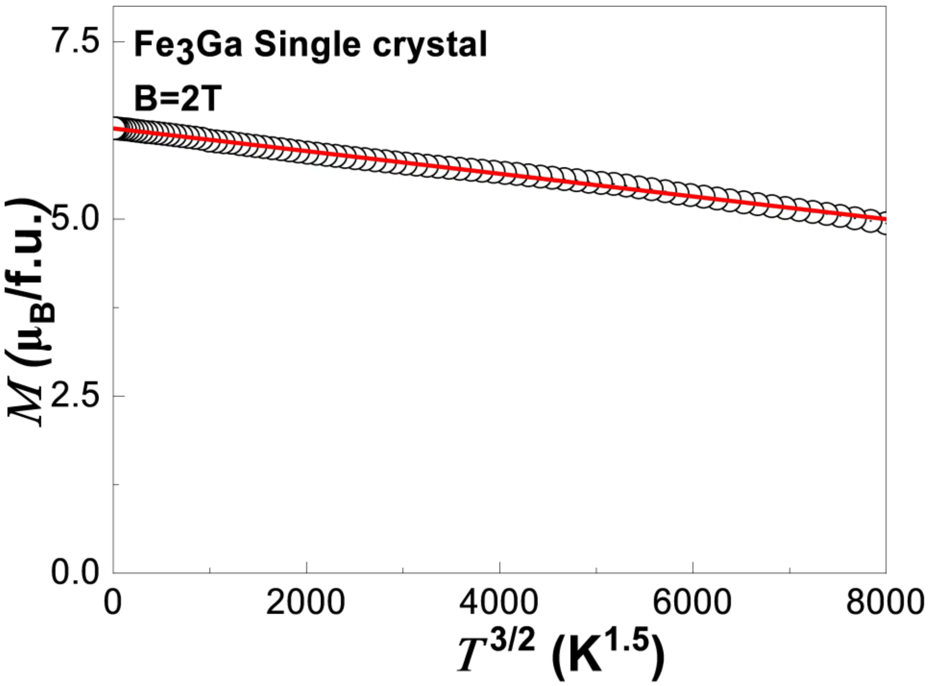

Supplementary Fig. 7. Magnetization changing with $\boldsymbol{T}^{3/2}$. Below 400 K, the saturated magnetization changing with the temperature in the Bloch's $\boldsymbol{T}^{3/2}$ law[24,25], namely $\boldsymbol{M} = \boldsymbol{M}_0 - \alpha \boldsymbol{T}^{3/2}$, strongly supporting the large NMR above 50 K resulting from the scattering between electrons and spin-fluctuation.

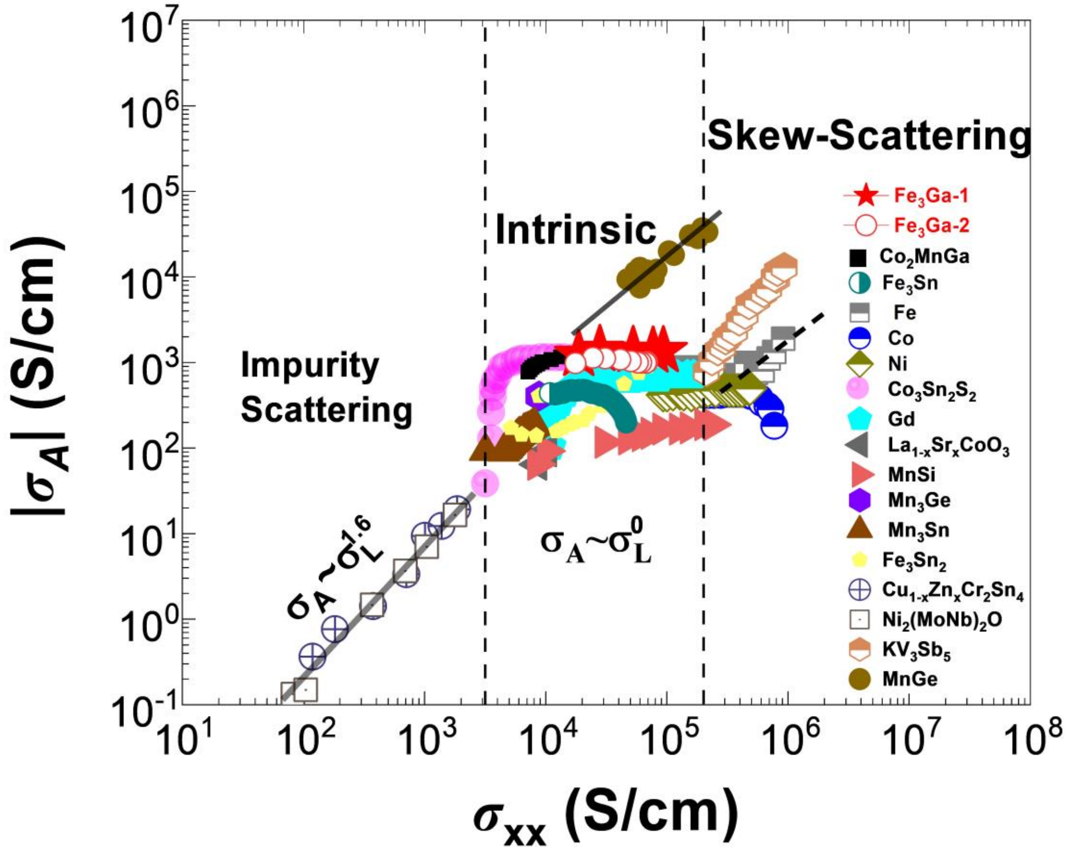

Supplementary Fig. 8. The scaling plot for the anomalous Hall conductivity and longitudinal conductivity.

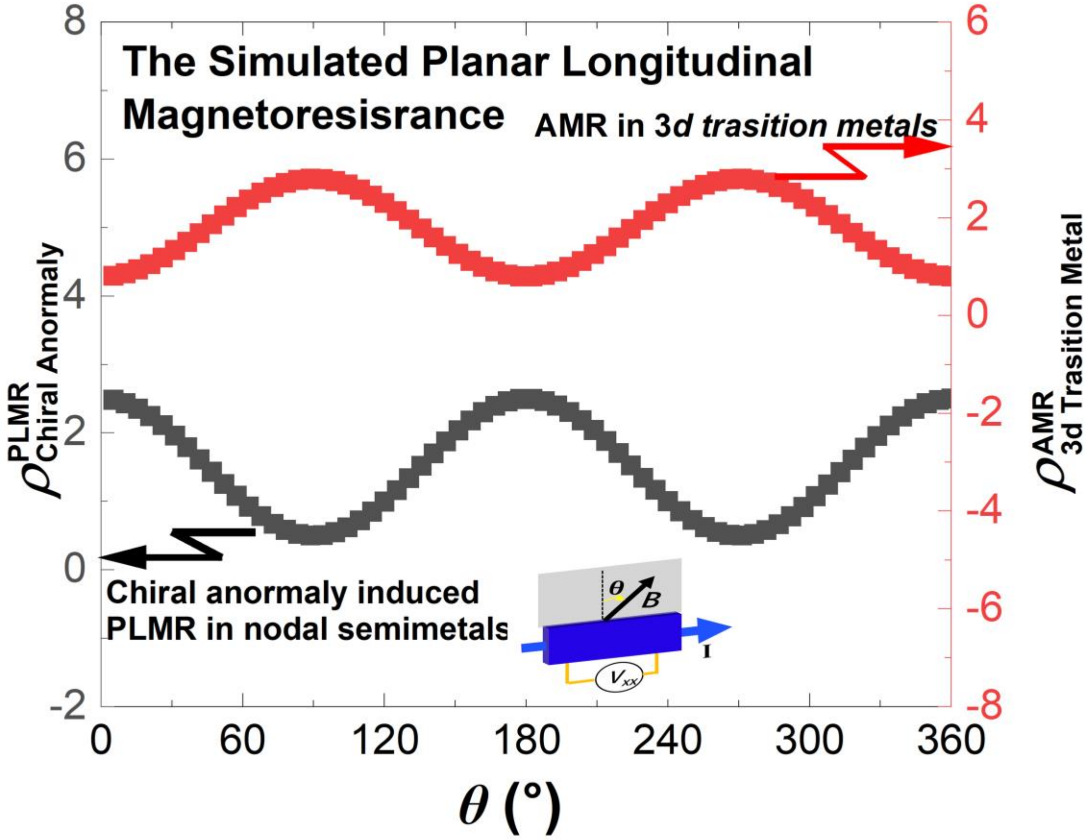

Supplementary Fig. 9. The simulated $\rho^{PLMR}_{chiral\ anomaly}$ and $\rho^{AMR}_{3d\ Transition\ Metal}$ based on the formula (S5) and (S6), respectively. The inset shows the configuration.

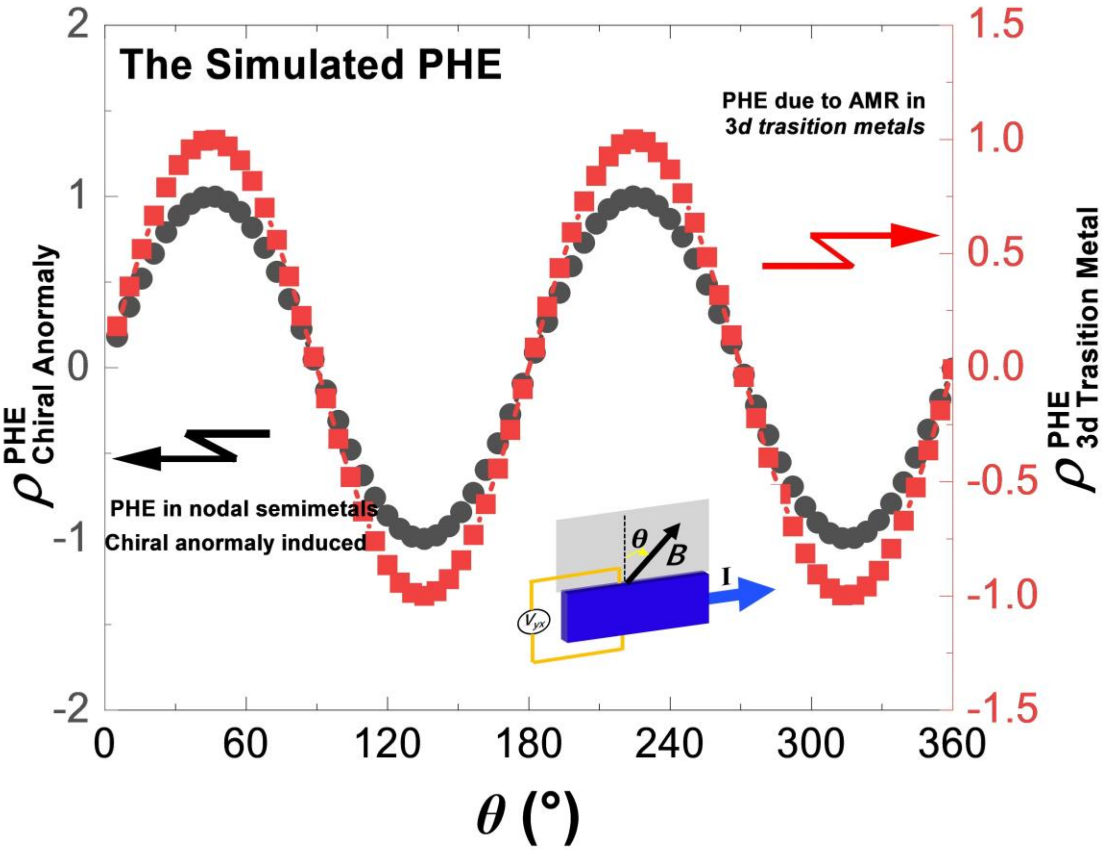

172

173 **Supplementary Fig. 10. The simulated $\rho^{PHE}_{Chiral\ Anormaly}$ and $\rho^{PHE}_{3d\ Transition\ Metal}$ induced by the chiral**
174 **anormal and AMR. The inset shows the configuration.**

175

176

Table S1.

The estimated τ_A from the previous literatures, using the formula (S2) in the Supplementary

Nodal Semimetals	Type	μ_B ($m^2 \cdot V^{-1} \cdot s^{-1}$)	E_F (meV)	V_F (m/s)	σ_{xx}^{χ} ($\Omega^{-1} \cdot m^{-1}$)	τ_a (s)	Reference (s)
Cd_3As_2	Dirac	900	232	9.3×10^5	1.67×10^6	1.19×10^{52}	[25]
Na_3Bi	Dirac	3.5	30	8.05×10^5	1.56×10^7	2.58×10^{48}	[26]
NbP	Weyl	500	98	4.8×10^5	1.59×10^8	2.53×10^{54}	[27]
TaAs	Weyl	50	11.48	1.16×10^5	1.87×10^6	2.11×10^{52}	[28]
WTe_2	Weyl-II	3.5	244.5	3.09×10^5	9.98×10^7	2.92×10^{50}	[29-31]
$Co_3Sn_2S_2$	Weyl	~0.074	12.3,5.9	$\sim26.6\times10^4$	4.2×10^4	$\sim2.26\times10^{45}$	[12]
Co_2MnGa	Nodal Line, Weyl	0.0035	80	2.7×10^4	2.75×10^4	4.33×10^{43}	[32,33]
Fe_3Ga	Nodal web	0.433-0.001	74	$<3\times10^8$	9.2×10^4	$>10^{30}$	[7] and this work

References and Notes

1. Nagaosa, N., Sinova, J., Onoda, S., MacDonald, A. H., & Ong, N. P. Anomalous Hall effect. *Rev. Mod. Phys.* 82, 1539–1592 (2010).
2. Xiao, D., Chang, M. C., & Niu, Q. Berry phase effects on electronic properties. *Rev. Mod. Phys.* 82, 1959–2007 (2010).
3. Nakatsuji, S., Kiyohara, N., & Higo, T. Large anomalous Hall effect in a non-collinear antiferromagnet at room temperature. *Nature* 527, 212–215 (2015).
4. Nayak, A. K. et al. Large anomalous Hall effect driven by a nonvanishing Berry curvature in the noncolinear antiferromagnet Mn_3Ge. *Sci. Adv.* 2, e1501870 (2016).
5. Fang, Z. et al. The anomalous Hall effect and magnetic monopoles in momentum space. *Science* 302, 92–95 (2003).
6. Chen, T. et al. Large anomalous Nernst effect and nodal plane in an iron-based kagome ferromagnet. *Sci. Adv.* 8, eabk1480 (2022).
7. Sakai, A. et al. Iron-based binary ferromagnets for transverse thermoelectric conversion. *Nature* 581, 53–57 (2020).
8. Železný, J., Yahagi, Y., Gomez-Olivella, C., Zhang, Y., & Sun, Y. High-throughput study of the anomalous Hall effect. *npj Comput. Mater.* 9, 151 (2023).
9. Xu, Y. et al. High-throughput calculations of magnetic topological materials. *Nature* 586, 702–707 (2020).
10. Noky, J. et al. Giant anomalous Hall and Nernst effect in magnetic cubic Heusler compounds. *npj Comput. Mater.* 6, 77 (2020).
11. Nagaosa, N. Anomalous Hall effect—A new perspective. *J. Phys. Soc. Jpn.* 75, 042001 (2006).
12. Liu, E. K. et al. Giant anomalous Hall effect in a ferromagnetic Kagome-lattice semimetal. *Nat. Phys.* 14, 1125–1131 (2018).
13. Scanlon, D. O. et al. Controlling bulk conductivity in topological insulators: Key role of anti-site defects. A*dv. Mater.* 24, 2154–2158 (2012).
14. Burkov, A. A. Negative longitudinal magnetoresistance in Dirac and Weyl metals. *Phys. Rev.* B 91, 245157 (2015).
15. Ong, N. P., & Liang, S. H. Experimental signatures of the chiral anomaly in Dirac-Weyl semimetals. *Nat. Rev. Phys.* 3, 394–404 (2021).
16. Liang, S. H. et al. Experimental tests of the chiral anomaly magnetoresistance in the Dirac-Weyl semimetals Na_3Bi and GdPtBi. *Phys. Rev. X* 8, 031002 (2018).
17. Xiong, J. et al. Evidence for the chiral anomaly in the Dirac semimetal Na_3Bi. *Science* 350, 413–416 (2015).
18. Huang, X. C. et al. Observation of the chiral-anomaly-induced negative magnetoresistance in 3D Weyl semimetal TaAs. *Phys. Rev. X* 5, 031023 (2015).
19. Burkov, A. A., Hook, M. D., & Balents, L. Topological nodal semimetals. *Phys. Rev. B* 84, 235126 (2011).
20. Son, D. T., & Spivak, B. Z. Chiral anomaly and classical negative magnetoresistance of Weyl metals. *Phys. Rev. B* 88, 104412 (2013).
21. McGuire, T., & Potter, R. Anisotropic magnetoresistance in ferromagnetic 3d alloys. IEEE Trans. Magn. 11, 1018–1038 (1975).
22. Florio, G. in Encyclopedia of Smart Materials (Ed. Olabi, A.-G.) 24–31 (Elsevier, Oxford, 2022).
23. Burkov, A. A. Giant planar Hall effect in topological metals. *Phys. Rev. B* 96, 041110 (2017).
24. Brommer, P. E. in Encyclopedia of Materials: *Science and Technology* (Eds. Buschow, K. H. J. et al.) 1–6 (Elsevier, Oxford, 2005).
25. Liang, T. et al. Ultrahigh mobility and giant magnetoresistance in the dirac semimetal Cd_3As_2. *Nature Mater.* 14, 280–284 (2015).
26. Xiong, J. et al. Anomalous conductivity tensor in the Dirac semimetal Na_3Bi. *Europhys. Lett.* 114, 27002 (2016).

27. Shekhar, C. et al. Extremely large magnetoresistance and ultrahigh mobility in the topological Weyl semimetal candidate NbP. *Nat. Phys.* 11, 645–649 (2015).
28. Zhang, C. L. et al. Tantalum Monoarsenide: an Exotic Compensated Semimetal. *arXiv:* 1502.00251 (2015).
29. Ali, M. N. et al. Large, Non-saturating magnetoresistance in WTe_2. *Nature* 514, 205–208 (2014).
30. Li, P. et al. Evidence for topological type-II Weyl semimetal WTe_2. *Nat. Commun.* 8, 2150 (2017).
31. Wang, Y. L. et al. Origin of the turn-on temperature behavior in WTe_2. *Phys. Rev. B* 92, 180402 (2015).
32. Sakai, A. et al. Giant anomalous Nernst effect and quantum-critical scaling in a ferromagnetic semimetal. *Nat. Phys.* 14, 1119–1124 (2018).
33. Belopolski, I. et al. Discovery of topological Weyl fermion lines and drumhead surface states in a room temperature magnet. *Science* 365, 1278–1281 (2019).